

# Berry curvature inside parity-time-symmetry protected exceptional surface

P. Wang,<sup>1</sup> L. Jin,<sup>2,\*</sup> and Z. Song<sup>2,†</sup>

<sup>1</sup>*Department of Mathematics and Physics, North China Electric Power University, Beijing 102206, China*

<sup>2</sup>*School of Physics, Nankai University, Tianjin 300071, China*

A three-dimensional non-Hermitian Hamiltonian with parity-time symmetry can exhibit a closed exceptional surface (EP surface) in momentum space, which is a non-Hermitian deformation of the degeneracy line (DL). Since the degeneracy line lacks an internal space, the distributions of Berry curvature inside the EP surface becomes particularly intriguing. This paper studies the distributions taking a torus-like EP surface as an example. In a meridian cross-section, the Berry connection exhibits a vortex-like field with only angular components, while the Berry curvature is perpendicular to this cross-section; in an equatorial cross-section, the Berry curvature forms a closed curve surrounding the central genus. Both Berry connection and curvature converge along the coplanar axis and diverge at the surface. We find the Berry flux depends on the radius of the integration region and is not quantized inside the EP torus. Approaching the surface, the Berry flux tends to infinity and the dynamical phase oscillates violently. We point that the streamlines of Berry curvature can be used to estimate the zero or non-zero Berry flux. We generalize the above patterns to the case of EP surfaces with complex shapes, and present a proposal of realizing the EP surface in an electrical circuit. Our research outcomes enhance the comprehension of EP surfaces and the topological characteristics of non-Hermitian systems with parity-time ( $PT$ ) symmetry.

## I. INTRODUCTION

The complex band structure and non-orthogonal eigenmodes induced by non-Hermiticity exhibit numerous intriguing properties [1–10]. The non-Hermitian phase transition occurs at the exceptional point (EP) where two or more eigenstates coalesce. The EP is unique and causes many exotic phenomena, such as polynomially increasing power [11–14] and sensitive dynamics near the EPs [15–22]. Considerable attention has been focused on the non-Hermitian topological phase. In Hermitian systems, the appearance of edge states [23] depends on the topological properties of the bulk system, known as the bulk-boundary correspondence (BBC) [24]. In non-Hermitian systems, the BBC may be invalidated by the non-Hermiticity associated with the non-Hermitian skin effect [25–37]. Exotic edge modes localized on the single boundary and the topological number from a non-Bloch bulk predict the topological phase transitions of the corresponding non-Hermitian systems [38–42]. Methods for characterizing the topology of non-Hermitian bands are investigated [43–50]. A visualization of the topological properties is proposed [51–53]. The origin and properties of non-Hermitian edge modes are further studied [54, 55] and the symmetry and classification of topological phases are reestablished [56–65]. The non-Hermitian extension of Hermitian models exhibits alternative topological phases [66–74], including the non-Hermitian Aubry-Andre-Harper models [75, 76], the Su-Schrieffer-Heeger models [77–82], and the non-Hermitian disordered topological systems [83–87]. The Floquet topological phase [88–90] and quantum walks [91–93] are extended to non-Hermitian systems. The interplay between time-periodic

driving fields and the presence of gain, loss, or nonreciprocal effects can lead to the emergence of topological phases exclusive to non-Hermitian Floquet systems [94–98]. The deformation of the contour specific to a topological invariant is demonstrated to accommodate the non-Hermiticity of the underlying non-interacting Hamiltonian in question [99]. In addition, many studies have focused on the novel topological nature induced by non-Hermiticity [100–118].

The high dimensional EP structure is a noteworthy problem. Exceptional rings (EP rings) have been intensively discussed theoretically and experimentally [119–125]. An EP ring can be analogous to a vortex filament, and the curl field related to the vortex filament is equivalent to the Berry connection [122]. In three-dimensional (3D) momentum space, non-Hermitian Hamiltonians with combined parity and time reversal symmetry spontaneously meet conditions for the appearance of exceptional surfaces (EP surfaces) [126, 127]. The EP surface is stable as long as the protecting symmetry is preserved [128]. The EP surface inherits the topological properties of the degenerate line (DL); the nodal volume, which represents bulk Fermi arcs in 3D space, indicates the remarkable control of the density of states (DOS) [127]. The topological properties of the EP surface can also be characterized by  $Z_2$  topological invariants, and a stable zero-gap quasi-particle state is protected by symmetry and topology [126]. In a high-dimensional parameter space, a hypersurface where the system remains at an EP improves the robustness and enhances the sensitivity of EPs, and a non-Hermitian sensor can be designed on the basis of the hypersurface [129]. A non-Hermitian Bardeen-Cooper-Schrieffer (BCS) Hamiltonian with a weak complex interaction possesses an EP surface in the quasi-particle Hamiltonian, and non-Hermiticity induces the breaking down of superfluidity and exhibition of reentrant behavior [130]. The EP sur-

\* jinliang@nankai.edu.cn

† songtc@nankai.edu.cn

face affects magnetic responses in a Hubbard model; the sharp local density of states (LDOS) at the Fermi energy for sublattices with weak correlations results in the local magnetic susceptibility of strong sublattice dependence [131]. Experimentally, the EP surface can be observed on a magnon polariton platform, and the EP surface can be conveniently tuned to coalesce into an anisotropic exceptional saddle point [132].

Motivated by recent theoretical advances in non-Hermitian topological systems, we investigate the distribution of Berry curvature inside the EP surface. The Berry curvature is gauge-invariant and related to the topological properties of EP surfaces. In this paper, we investigate a two-band non-Hermitian system with parity-time ( $\mathcal{PT}$ ) symmetry and a closed EP surface in 3D momentum space. The general expression of the Berry curvature defined under the biorthogonal basis reveals that the EP surface separates the zero and non-zero Berry curvature. A Hamiltonian with a torus-like EP surface is exemplified. The topological properties of the EP surface are encoded in the distributions of the Berry curvature in the meridians and equatorial cross-sections. In the meridians cross-section, the Berry connection acts as a planar vortex field and the direction of the Berry curvature is perpendicular to this cross-section; in the equatorial cross-section, Berry curvatures form closed curves. Both Berry connection and curvature are convergent at the coplanar axis and divergent at the EP surface. The surface integral of the Berry curvature yields a non-quantized Berry flux. The numerical simulation implies that the non-quantized Berry flux is consistent with the dynamics phase accumulated in the adiabatic evolution, and both of them oscillates violently near the EP surface. The Berry flux can be evaluated by the distribution of Berry curvature. Berry flux is nonzero if the Berry curvatures have the same direction in the meridians cross-section otherwise vanishes. These patterns can be generalized to the EP surfaces with complicated geometries. Finally, rather than the realization in coupled resonators [133], we point that the EP surface can be measured in a electrical circuit.

The remainder of the paper is organized as follows: In Sec. II, we introduce the 3D  $\mathcal{PT}$ -symmetric non-Hermitian two-band system. In Sec. III, we present the formal expression of Berry connection and curvature. In Sec. IV, we introduce a concrete model to exhibit the Berry curvature inside a torus-like EP surface. The non-quantized Berry flux is elucidated from the distribution of the Berry curvature. In Sec. V, the adiabatic evolution is implemented. In Sec. VI, a topological system that possesses more complicated EP surface is further discussed. In Sec. VII, the proposal of realizing the EP surface is given in the electrical circuits. In Sec. VIII, we summarize the results.

## II. NON-HERMITIAN TWO-BAND SYSTEM

We consider a non-Hermitian two-band Hamiltonian in the momentum space  $\mathbf{k} = \{k_x, k_y, k_z\}$ ,

$$h_{\mathbf{k}} = \mathbf{B}(\mathbf{k}) \cdot \boldsymbol{\sigma}, \quad (1)$$

where  $\boldsymbol{\sigma} = \{\sigma_x, \sigma_y, \sigma_z\}$  is the Pauli matrix; the component  $\{B_x(\mathbf{k}), B_y(\mathbf{k})\}$  of the auxiliary field  $\mathbf{B}(\mathbf{k})$  is the real and periodic function of  $k = \{k_x, k_y, k_z\}$ ; and the other component  $B_z = i\gamma$  is a constant, which is introduced as the gain and loss.  $h_{\mathbf{k}}$  possesses the  $\mathcal{PT}$ -symmetry  $[\mathcal{PT}, h_{\mathbf{k}}] = 0$ , where  $\mathcal{P} = \sigma_x$  is the parity operator and  $\mathcal{T}$  is the time-reversal operator that  $\mathcal{T}^{-1}i\mathcal{T} = -i$ . The eigenvalues of  $\mathcal{PT}$ -symmetric systems are either real numbers or complex conjugate pairs respectively associated with  $\mathcal{PT}$ -symmetry unbroken or broken eigenstates, respectively. Considering the specific form of the band in Eq. (1), i.e.  $\pm\sqrt{B_x^2 + B_y^2 - \gamma^2}$ , the complex conjugate pairs are reduced to purely imaginary numbers. The eigenstate expressions involve parameters defined in terms of energy, therefore the real/imaginary eigenvalues make the expressions more concise. In addition,  $h_{\mathbf{k}}$  is the pseudo anti-Hermitian  $\sigma_z h_{\mathbf{k}} \sigma_z^{-1} = -h_{\mathbf{k}}^\dagger$  [134]. It is straightforward to check that  $h_{\mathbf{k}}^\dagger \sigma_z |\phi\rangle = -\varepsilon \sigma_z |\phi\rangle$ , where  $h_{\mathbf{k}} |\phi\rangle = \varepsilon |\phi\rangle$ . This implies that  $\sigma_z |\phi\rangle$  becomes the left eigenstate corresponding to the right eigenstate  $|\phi\rangle$  when  $\varepsilon$  is purely imaginary. These characteristics of  $h_{\mathbf{k}}$  simplify the calculations in the following text and are reflected in Sec. III.

In the Hermitian case ( $\gamma = 0$ ), the band degeneracy is determined by the following equations

$$B_x(\mathbf{k}) = B_y(\mathbf{k}) = 0. \quad (2)$$

$B_x(\mathbf{k}) = 0$  and  $B_y(\mathbf{k}) = 0$  each represent a surface in the 3D momentum space. The intersection of two surfaces is the degeneracy line (DL). The topological properties of the DL are captured by the topological number Berry flux or winding number. The former is the integral of the Berry connection on a closed circle, while the latter is obtained by dividing the Berry flux by  $\pi$ . The Berry flux is quantized to  $\pi$  (0) if the closed circle is (not) linked with the DL [135, 136]. In the presence of gain and loss for  $\gamma \neq 0$ , the DL becomes an EP surface. The EP surface is the zero-energy surface in the form of

$$\gamma^2 = B_x^2(\mathbf{k}) + B_y^2(\mathbf{k}). \quad (3)$$

We consider the case in which Eq. (3) describes a closed 2D surface in the 3D momentum space at the selected  $\{B_x(\mathbf{k}), B_y(\mathbf{k})\}$ . In this situation, the energy is real outside the closed EP surface and is purely imaginary inside the closed EP surface. We regard the purely imaginary region as the nodal volume wrapped by the EP surface. These data serve as the 3D bulk Fermi arcs [127].  $\mathcal{PT}$ -symmetry protects the EP surface which inherits the Berry flux of the DL [126, 127]. In this work, we focus on the Berry curvature distributions inside and outside the EP surface.

### III. BERRY CONNECTION AND BERRY CURVATURE

This section provides the general expressions of Berry connections and curvatures inside and outside the EP surface.

We first calculate the eigenstates of the Bloch Hamiltonian under biorthogonal norm. The right eigenstates  $|\phi_{\pm}^{\text{R}}\rangle$  of the Bloch Hamiltonian satisfy  $h_{\mathbf{k}}|\phi_{\pm}^{\text{R}}\rangle = \varepsilon_{\pm}|\phi_{\pm}^{\text{R}}\rangle$  and the left eigenstates  $|\phi_{\pm}^{\text{L}}\rangle$  satisfy  $h_{\mathbf{k}}^{\dagger}|\phi_{\pm}^{\text{L}}\rangle = \varepsilon_{\pm}^*|\phi_{\pm}^{\text{L}}\rangle$ . They are normalized under the biorthogonal norm  $\langle\phi_{\alpha}^{\text{L}}|\phi_{\alpha}^{\text{R}}\rangle = 1$  ( $\alpha = +/-$ ). The EP surface serves as a boundary separating the real and complex energies. The Bloch Hamiltonian possesses an entirely real spectrum outside the EP surface (i.e. the  $\mathcal{PT}$ -symmetry unbroken phase) and possesses an entirely imaginary spectrum inside the EP surface (i.e. the  $\mathcal{PT}$ -symmetry broken phase). For the geometric features of the lower band  $|\phi_{-}^{\text{R}}\rangle$  with energy  $-\sqrt{B_x^2 + B_y^2 - \gamma^2}$ , in the unbroken  $\mathcal{PT}$ -symmetry region  $\gamma^2 < B_x^2 + B_y^2$ , the right and left eigenstates are in the form

$$|\phi_{-}^{\text{R}}\rangle = [e^{i(-\alpha-\beta)}, 1]^{\text{T}} \leftrightarrow -\varepsilon, \quad (4)$$

$$|\phi_{-}^{\text{L}}\rangle = [e^{i(\alpha-\beta)}, -1]^{\text{T}}/\Omega \leftrightarrow -\varepsilon, \quad (5)$$

respectively, where  $\varepsilon = \sqrt{B_x^2 + B_y^2 - \gamma^2}$ ,  $\alpha$  and  $\beta$  are determined by  $\tan \alpha = \gamma/\varepsilon$  and  $\tan \beta = B_y/B_x$  respectively, and  $\Omega = -2ie^{i\alpha}\sin \alpha$ . In the broken region  $\gamma^2 > B_x^2 + B_y^2$ , the right and left eigenstates are in the form

$$|\phi_{-}^{\text{R}}\rangle = [\eta e^{i(\frac{\pi}{2}-\beta)}, 1]^{\text{T}} \leftrightarrow -i\varepsilon, \quad (6)$$

$$|\phi_{-}^{\text{L}}\rangle = [-\eta e^{i(\frac{\pi}{2}-\beta)}, 1]^{\text{T}}/\Omega \leftrightarrow i\varepsilon, \quad (7)$$

respectively, where  $\varepsilon = \sqrt{\gamma^2 - B_x^2 - B_y^2}$ ,  $\eta = (\gamma - \varepsilon)/\sqrt{B_x^2 + B_y^2}$ , and  $\Omega = 2\eta\varepsilon/\sqrt{B_x^2 + B_y^2}$ .

The Berry connection is defined as  $\vec{\mathcal{A}} = \text{Re}(i\langle\phi_{\pm}^{\text{L}}|\vec{\nabla}|\phi_{\pm}^{\text{R}}\rangle)$  and the Berry curvature is defined as  $\vec{\mathcal{F}} = \vec{\nabla} \times \vec{\mathcal{A}}$ , where  $\vec{\nabla} = \partial_{k_x}\hat{e}_x + \partial_{k_y}\hat{e}_y + \partial_{k_z}\hat{e}_z$ . Therefore, the formal expressions of the Berry connection and Berry curvature differ between the unbroken and broken  $\mathcal{PT}$ -symmetric phases. The Berry connection is complex in both the broken and unbroken regions, the imaginary part amplifies the Dirac probability of the adiabatic evolved state, whereas the real part is related to the topological properties of the system [137]. Therefore, we consider only the real part of the Berry connection in the definition. The detailed calculations are provided in the Appendix, and the results are presented concisely as follows.

Inside the EP surface  $\mathcal{PT}$ -symmetry is broken. The components of Berry connection  $\mathcal{A}_j$  and Berry curvature

$\mathcal{F}_j$  read

$$\mathcal{A}_j = \frac{(\varepsilon - \gamma)(B_x\partial_j B_y - B_y\partial_j B_x)}{2\varepsilon(B_x^2 + B_y^2)}, \quad (8)$$

$$\mathcal{F}_j = \frac{\gamma(\partial_l B_y\partial_l B_x - \partial_l B_x\partial_l B_y)}{2\varepsilon^3}, \quad (9)$$

where  $\partial_j = \partial/\partial k_j$  ( $j = x, y, z$ ) and  $\varepsilon = \sqrt{\gamma^2 - B_x^2 - B_y^2}$ .  $\mathcal{A}_j$  and  $\mathcal{F}_j$  converge at the DL in the Hermitian case (i.e.,  $B_x = B_y = 0$  or  $\varepsilon = 0$ ) and are infinite at the singularity  $\varepsilon = 0$  (i.e., the EP surface).

Outside the nodal volume the  $\mathcal{PT}$  symmetry holds. The Berry connection and Berry curvature become

$$\mathcal{A}_j = \frac{(\gamma B_x - \varepsilon B_y)\partial_j B_x + (\varepsilon B_x + \gamma B_y)\partial_j B_y}{2\varepsilon(B_x^2 + B_y^2)}. \quad (10)$$

$$\vec{\mathcal{F}} = 0. \quad (11)$$

Equations (9) and (11) imply that the EP surface acts as the boundary between zero and non-zero Berry curvature. To extract more explicit information on the Berry connection and curvature, we further simplify these formulas inside a torus-like EP surface.

### IV. TORUS-LIKE EP SURFACE

We use a concrete model possessing an EP surface to study the distributions of Berry connection and curvature in the broken region, from which the inheritance of the Berry flux is well interpreted. The auxiliary field  $\mathbf{B}(\mathbf{k}) = \{B_x, B_y\}$  of the concrete Hamiltonian is in the form

$$\begin{cases} B_x = f(k_x, k_y) - s \cos k_z \\ B_y = s \sin k_z \end{cases}, \quad (12)$$

where  $f(k_x, k_y) = m - a \cos k_x - a \cos k_y$ , and  $s = 1$ . The physical realization of the concrete Hamiltonian is proposed [127, 138].

The general geometric property of the EP surface is determined by the components  $\{B_x(\mathbf{k}), B_y(\mathbf{k})\}$ . Equations (2), (3), and (12) indicate there are two identical nodal volumes located at the  $k_z = 0$  and  $k_z = \pi$  planes, only the former is studied for convenience. With fixed parameters  $\{m, a\}$ , Eq. (3) implies that the maximum of  $B_y$  is  $B_y = \gamma$  (i.e.,  $s \sin k_z = \gamma$ ) in the situation  $B_x = 0$ ; therefore, the maximum of  $k_z$  on the EP surface is  $k_{z\text{max}} = \arcsin(\gamma/s)$ , and the restriction  $\gamma < 1$  is imposed. In fact, if  $\gamma = 1$ , the two EP surfaces touch at  $k_{z\text{max}} = \arcsin \gamma$ . In addition, the EP surface possesses a mirror symmetry with respect to the  $k_z = 0$  plane.

The system possesses a torus-like EP surface under the appropriate parameters (see Sec. VIII B). A schematic diagram of the torus-like EP surface is shown in Fig. 1(a). The red coplanar circular axis is DL in the Hermitian case. Two types of cross-sections are studied in this

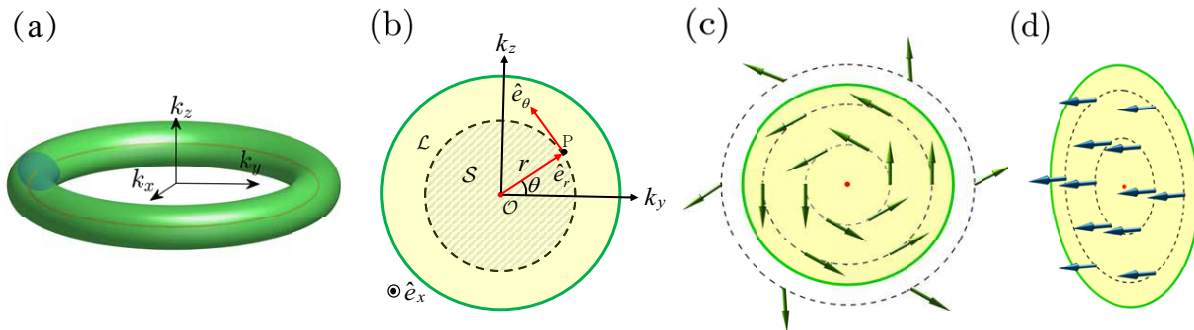


FIG. 1. (a) Torus EP surface (green) at  $\gamma = 0.05$ ,  $a \approx 3.2$ ,  $m \approx 4.05$ . The dark disk is the representative cross-section  $S_V$  and the red co-planar circular axis is the DL. (b) Schematic diagram of the cross-section  $S_V$ . (c) Berry connection and (d) Berry curvature in the cross-section  $S_V$ .

paper, i.e., meridional (equatorial) cross-sections in the form of closed disks (annulus). The meridional (equatorial) cross-sections represent the intersection of the nodal volume and the vertical plane passing through the origin (equatorial plane). For convenience, a cross-section denoted  $S_V$  ( $S_H$ ) as the intersection of the nodal volume and the  $k_y O k_z$  ( $k_x O k_y$ ) plane is chosen as a representative meridian (equatorial). Schematic diagrams of  $S_V$  and  $S_H$  are shown in Fig. 1(b) and Fig. 2 respectively. The distributions of Berry curvature and Berry connection in the other cross-sections are similar to those in  $S_V$  and  $S_H$ . Therefore, the distributions of berry curvature and berry connection inside the nodal volume can be obtained once the distribution is given in the two representative cross-sections.

### A. Distribution in the meridional cross-section

This section discusses the distribution of Berry curvature in the cross-section  $S_V$  of the concrete model in Eq. (12).

In the cross-section  $S_V$ , polar coordinates are used to describe the physical quantities. As shown in Fig. 1(b), the green EP ring divides the plane into two parts: the Hamiltonian has an entirely imaginary spectrum in the yellow region inside the EP ring and an entirely real spectrum outside the EP ring. The EP ring is subcircular with radius  $\gamma$ . The circular dashed line is the energy contour  $\mathcal{L}$  with radius  $r$ . The red point  $O(0, k_{y0}, 0)$  is center of the  $S_V$  and is the degenerate point (DP) in the Hermitian case ( $\gamma = 0$ ). The arbitrary point  $P(0, k_y, k_z)$  on the contour  $\mathcal{L}$  can be rewritten as  $P(0, r, \theta)$  in the cylindrical coordinate system, where  $\theta$  is the included angle between position vector  $P$  and coordinate axis  $k_y$ . The three unit vectors  $\{\hat{e}_\theta, \hat{e}_r, \hat{e}_x\}$  of the cylindrical coordinate system are presented. Under the parameter settings given in Sec. VIII B, the Hamiltonian in the cross-section  $S_V$  is reduced to

$$H = \begin{pmatrix} i\gamma & r e^{i\theta} \\ r e^{-i\theta} & -i\gamma \end{pmatrix}. \quad (13)$$

It is straightforward to check that the reduced Hamiltonian  $H$  obeys the  $\mathcal{PT}$ -symmetry, i.e.,  $\mathcal{T}\sigma_x H (\mathcal{T}\sigma_x)^{-1} = H$ . For the case with complex matrices, a numerical result can be obtained, exhibiting a deformed but similar distribution of Berry curvature, as shown in Sec. VI.

The distributions of the Berry connection and Berry curvature in  $S_V$  are illustrated in Fig. 1(c) and (d). Inside the EP ring, the expression of the Berry connection at the position  $P(0, r, \theta)$  ( $r < \gamma$ ) in Eq. (8) is reduced to

$$\vec{\mathcal{A}} \approx \frac{\varepsilon - \gamma}{2\varepsilon r} \vec{e}_\theta \quad (0 \leq r < \gamma), \quad (14)$$

where  $\varepsilon = \sqrt{\gamma^2 - r^2}$ . The expression of the Berry connection in the above equation is equal to the expression directly calculated from Eq. (13). Equation (14) indicates that the radial component  $\vec{e}_r$  vanishes, and the angular component  $\vec{e}_\theta$  is non-zero, so  $\vec{\mathcal{A}}$  is a planar vortex field. We show the direction of  $\vec{\mathcal{A}}$  by the arrows without considering its intensity according to Eq. (14), and each arrow is tangent to the energy contour  $\mathcal{L}$ . It is not difficult to check that

$$\lim_{r \rightarrow 0} \frac{\sqrt{\gamma^2 - r^2} - \gamma}{2\sqrt{\gamma^2 - r^2} r} = 0, \quad (15)$$

which indicates that  $\vec{\mathcal{A}}$  converges at  $r = 0$  (i.e., DP at  $\gamma = 0$ ).  $\vec{\mathcal{A}}$  is divergent at  $\varepsilon = 0$ . Equation (9) can be reduced to

$$\vec{\mathcal{F}} \approx \frac{\gamma}{2\sqrt{\gamma^2 - r^2}} \vec{e}_x \quad 0 \leq r < \gamma \quad (16)$$

inside the EP ring. The expression for the Berry curvature in the above equation is equal to the expression directly calculated from Eq. (13). Equation (16) indicates that only the axial component  $\vec{e}_x$  is non-zero. The Berry curvature has a divergent value at  $r = \gamma$  (i.e. the EP ring) and a convergent value at  $r = 0$ . In Fig. 1(d), we exhibit the direction of  $\vec{\mathcal{F}}$ . As we can see, all the arrows in  $S_V$  point in the same direction, which is the normal



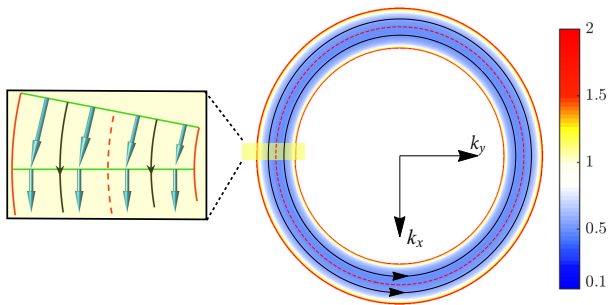


FIG. 2. Streamlines of Berry curvature in the equatorial cross-section. Inset: top view of Berry curvature in  $S_V$  cross-section and its adjacent cross-section.

of  $S_V$ . As an analogy, these arrows can be regarded as magnetic field lines, and the total magnetic flux is the number of magnetic field lines that pass through  $S_V$ . In addition, in two adjacent meridional cross-sections, these arrows are connected end to end, as shown in the inset of Fig. 2, where the green solid lines denote the top view of meridional cross-sections; and the dashed red line is the DL in the Hermitian case ( $\gamma = 0$ ). The arrows in all the meridional cross-sections form a closed curve (see Fig. 2).

The Berry flux is related to the distribution of the Berry curvature or Berry connection and can be used to capture the topological nature of the EP surface,

$$\Phi_{\mathbf{B}} = \oint_{\mathcal{L}} \vec{A} \cdot d\vec{l}_k = \iint_{\mathcal{S}} \vec{\mathcal{F}} \cdot d\vec{\mathcal{S}}, \quad (17a)$$

where  $\mathcal{S}$  is the integral surface, which is the shaded region surrounded by  $\mathcal{L}$  presented in Fig. 1(b). By substituting Eq. (16) into Eq. (17a), we can obtain

$$\Phi_{\mathbf{B}} = \pi - \frac{\gamma\pi}{\sqrt{\gamma^2 - r^2}}. \quad (18)$$

$\Phi_{\mathbf{B}}$  is divergent on the EP surface ( $r = \gamma$ ). Therefore the geometric phase oscillates sharply when the integration path approaches the EP surface. Due to the divergence of the Berry connection and curvature on the exceptional point (EP) surface, the line integral of the Berry curvature will not be equal to the surface integral of the Berry curvature when the integration path is located in the unbroken region, that is, the Stokes theorem does not hold. In addition, the Berry flux can be regarded as the total magnetic flux. In Fig. 1(d), the uniform pointing of the arrows indicate that the same sign contributes to the Berry flux and therefore a non-zero Berry flux.

## B. Distribution in the equatorial cross-section

This section investigates the distribution of the Berry curvature in  $S_H$ .

In the equatorial cross-section  $S_H$ , the Berry curvature in Eq. (9) inside the EP ring is reduced to

$$\begin{cases} \mathcal{F}_x = s\gamma\partial_y B_x / (2\varepsilon^3) \\ \mathcal{F}_y = -s\gamma\partial_x B_x / (2\varepsilon^3) \\ \mathcal{F}_z = 0 \end{cases}, \quad (19)$$

Therefore, the orientation of the Berry curvature at an arbitrary point  $(k_x, k_y, 0)$  in  $S_H$  is  $\mathcal{F}_y/\mathcal{F}_x = -(\partial_x B_x)/(\partial_y B_x)$ . In addition Eq. (3) can be reduced to

$$B_x(k_x, k_y, 0) = \gamma', \quad (20)$$

in  $S_H$  where  $|\gamma'| \leq |\gamma|$ . Equation (20) represents a closed curve inside the equatorial cross-section for a fixed  $\gamma'$ . This closed curve is the intersection between the  $k_z = 0$  plane and the EP surface and is determined by replacing  $\gamma$  with  $\gamma'$  ( $|\gamma'| < |\gamma|$ ) in Eq. (3). If  $\gamma' = \gamma$ , the curve is the EP ring as well as the periphery of  $S_H$ . If  $\gamma'$  changes from  $-\gamma$  to  $\gamma$ , all the curves determined by every  $\gamma'$  constitute the equatorial cross-section, and no two curves have a crossing point. The tangent of a curve at  $(k_x, k_y, 0)$  is  $dk_y/dk_x = -(\partial_x B_x)/(\partial_y B_x)$  as a result of complete differentiation on both sides of Eq. (20). Compared with the equation  $\mathcal{F}_y/\mathcal{F}_x = -(\partial_x B_x)/(\partial_y B_x)$ , we conclude that the direction of Berry curvature at the point  $(k_x, k_y, 0)$  is identical to the tangent of the curve passing through this point,

$$\mathcal{F}_y/\mathcal{F}_x = dk_y/dk_x. \quad (21)$$

The above results hold true as long as  $B_y$  is a function of only  $k_z$ .

The streamlines of the Berry curvature in  $S_H$  according to Eq. (20) are shown in Fig. 2. A different closed black curve is depicted by setting different  $\gamma'$ . The red solid EP lines ( $\gamma' = \gamma$ ) serve as the boundary separating non-zero and zero Berry curvatures; the region between the two EP lines has non-zero Berry curvature. The dashed red line ( $\gamma' = 0$ ) represents the DL for the Hermitian case. The black curves ( $0 < \gamma' < \gamma$ ) with arrows represent the orientation of the Berry curvature, and the background color indicates the intensity of the Berry curvature. The intensity values are shown in the color bar. The Berry curvature approached infinity near the EP lines. The streamlines surrounding the hole flow anticlockwise. All the streamlines of the Berry curvature are closed, which coincides with the equation  $\nabla \cdot \vec{\mathcal{F}} = 0$ , meaning that Berry curvatures act as a field without sources. In addition, Eq. (21) can be generalized to the other intersection between the  $k_z = k_{z'}$  plane and the EP surface. The distributions claim a clear physical correspondence for the Berry curvature and EP surface. The Berry curvature can be analogous to magnetic lines generated by a solenoid, and the EP surface can be connected to this solenoid. The total magnetic flux is the number of magnetic field lines passing through certain cross-section.

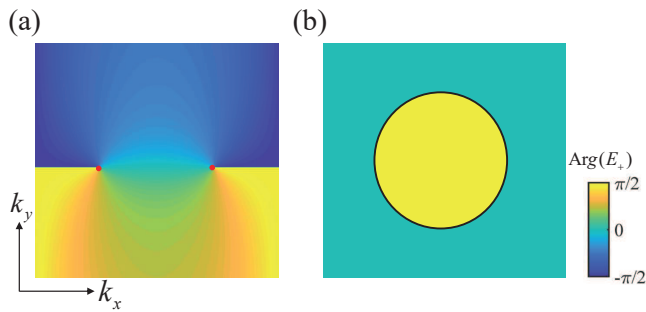


FIG. 3. (a) Plot of  $\text{Arg}(E_+ - E_-)$  for two isolated EPs. The two red points represent two isolated EPs (i.e., two vortices). (b) Plots of  $\text{Arg}(E_+ - E_-)$  for EP surface. The black line represents the EL (i.e., a cross-section of EP surface).

This section examined the distribution of the Berry curvature inside the EP surface using two types of cross-sections as examples, and calculates the Berry flux. Before moving on to the next section, there are three points that need to be supplemented and explained:

i) The above results are obtained under the biorthogonal basis sets. Under the Dirac basis sets, the directions of the Berry connection and Berry curvature at any point inside the EP surface are the same but the magnitudes are different, and the two kinds of Berry fluxes are different. Both the Berry connection and Berry curvature under the Dirac basis sets converge on the EP surface, therefore the Stokes theorem holds.

ii) The winding number associated with the berry connection cannot be used to capture the topological nature of the EP surface. Figure 1(c) shows the direction of  $\vec{A}$  denoted by arrows. The winding numbers of the arrows along the contour  $\mathcal{L}$  outside and inside the EP ring are both non-zero. However, this non-zero winding number is not related to the non-zero Berry flux. The Berry flux in Eq. (17a) can be rewritten as the loop integral of the Berry connection, i.e.  $\Phi_{\mathbf{B}} = \oint_{\mathcal{L}} \vec{A} \cdot d\vec{k}$ , and it is not equal to the expression of the winding number for the Berry connection  $W = (2\pi)^{-1} \oint_{\mathcal{L}} (\mathcal{A}_y \nabla \mathcal{A}_x - \mathcal{A}_x \nabla \mathcal{A}_y) / |\mathcal{A}|^2 d\mathbf{k}$ .

iii) There is an open question that is the topological connection between the isolated EPs and the EP surface in the context of topological number. The nontrivial topological nature of an isolated EP depends on the scalar field defined by the spectral phase  $\text{Arg}(E_+ - E_-)$  (see Fig. 3(a)) [44, 139]. The EP is regarded as a vortex of the scalar field where the spectral phase cannot be effectively defined. The topological nature of an EP can be characterized by the topological number  $\pi$  or  $1/2$ , the former is the spectral phase difference accumulated when encircling the vortex while the latter is the winding number obtained through dividing this phase difference by  $2\pi$ . Therefore EPs can be analogous to  $\pi$ -vortices, which hangs together with the topological defect in a nematic [140–144] or defects in TIs [145–149]. The isolated EPs may merge accompanied by the algebraic addition of topological numbers [150]. The subject of this

study is the EP surface, which is a collection of infinite EPs. Figure 3(b) exhibits the spectral phase of EP surface. There is no obvious evidence that the topological properties of EP surface are related to the spectral phase. Corresponding to the same spectral phase in Fig. 3(b), Figs. 1(d) and 5(f) exhibit two distinct distributions of Berry curvature. The above analyses indicate that the spectral phase cannot describe the topology of the EP surface completely, and the winding number corresponding to EP surface is also not equal to  $\pm 1/2$ . Therefore EP surface cannot be simply understood as the merger of isolated EPs. The topological connection between the EPs and EP surfaces deserves further investigation.

## V. ADIABATIC EVOLUTION

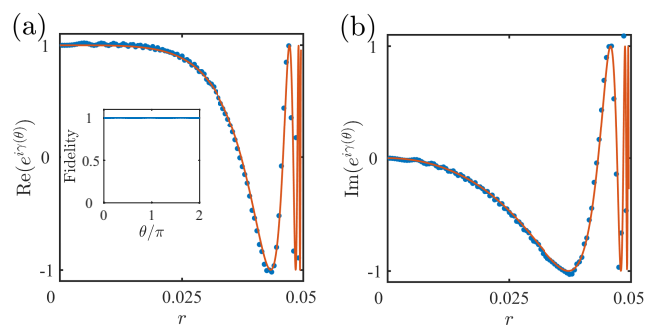


FIG. 4. Schematics of the geometric phase  $e^{i\gamma(\theta)}$ . (a) Real part and (b) imaginary part. The blue points are numerical results and the red solid line are analytical results according to Eq. (18). Inset: fidelity for  $r = \gamma/2$ . The parameters are the same as those in Fig. 1(a).

To verify the above results, we numerically simulate the adiabatic evolution driven by the Hamiltonian in Eq. (13) and compare the geometric phase obtained by numerical simulation and the analytical results in Eq. 18. Considering the adiabatic evolution on the circular contour  $\mathcal{L}$  with a radius  $r$  [see Fig. 1(b)].  $H$  in Eq. (13) is a periodic function of  $\theta$ ,  $H(\theta) = H(\theta + 2\pi)$ . The lower band eigenstate  $|\phi_{-}^{\text{R}}(0)\rangle$  reverts to  $|\phi_{-}^{\text{R}}(0)\rangle$  if  $\theta$  varies adiabatically from 0 to  $2\pi$ , and the evolved state is the instantaneous lower band eigenstate  $|\phi_{-}^{\text{R}}(\theta)\rangle$ . More explicitly, the adiabatic evolution of the initial state  $|\phi_{-}^{\text{R}}(0)\rangle$  under the Hamiltonian  $H(\theta)$  can be expressed as

$$\begin{aligned} |\Psi_{\lambda}^k(\theta)\rangle &= \mathcal{T} \exp[-i \int_0^{\theta} H(\theta) d\theta] |\phi(0)\rangle \\ &= e^{i(\alpha(\theta) + \gamma(\theta))} |\phi(0)\rangle, \end{aligned} \quad (22)$$

where the dynamic phase  $\alpha(\theta)$  and the adiabatic phase  $\gamma(\theta)$  have the form

$$\alpha(\theta) = - \int_0^{\theta} \varepsilon_k(\theta) d\theta, \gamma(\theta) = \int_0^{\theta} \mathcal{A}(\theta) d\theta. \quad (23)$$

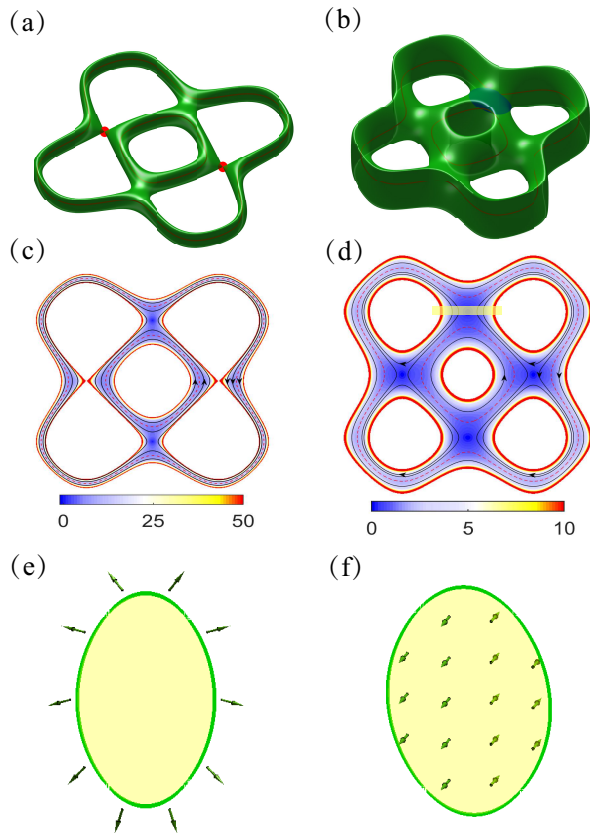


FIG. 5. Genus at parameters  $a = 2, b = 2.3, c = d = 2.8, m = 0.3$ , (a)  $\gamma = 109/140$  and (b)  $\gamma = 1.9$ . (c) and (d): Streamlines of Berry curvature in the equatorial cross-section for the configurations in (a) and (b), respectively. (e) and (f): Berry connection outside the EP ring and Berry curvature inside the EP ring on a specific cross-section, this specific cross-section is depicted in (b) and (d).

$\mathcal{A}(\theta)$  is presented in Eq. (14) and  $\gamma(\theta)$  is equivalent to the Berry flux in Eq. (18). The imaginary part of  $\mathcal{A}(\theta)$  in Eq. (39) vanishes due to the invariability  $\eta = (\gamma - \varepsilon)/\sqrt{\gamma^2 - \varepsilon^2}$  on the contour  $\mathcal{L}$  and therefore does not contribute to adiabatic evolution. However  $\alpha(\theta)$  is imaginary and the Dirac probability increases exponentially. To eliminate the exponential growth in probability induced by the imaginary dynamic phase, we add a factor  $i$  before the Hamiltonian  $H$  in the numerical simulation; consequently  $\alpha(\theta)$  becomes real and  $\gamma(\theta)$  is unaffected.

Figure. 4 numerically and analytically exhibits the geometric phase  $e^{i\gamma(\theta)}$  on the contour  $\mathcal{L}$  with  $r$  ranging from 0 to  $\gamma$  ( $r = \gamma$  indicates that  $\mathcal{L}$  is the EP ring). The numerical results correspond with the analytical calculations in Eq (18). The oscillating frequency of the real and imaginary parts of the geometric phase accelerates as the contour  $\mathcal{L}$  approaches the EP ring (i.e.,  $r = \gamma$ ). As a sample, the inset numerically presents the fidelity

when  $r = \gamma/2$ , which is defined as

$$F(\theta) = \left| \langle \phi_-^R(\theta) | \mathcal{T} \exp[-i \int_0^t H(\theta) d\theta] | \phi_-^R(0) \rangle \right|. \quad (24)$$

A fidelity of 1 indicates that the time evolution process is adiabatic.

## VI. EP SURFACE WITH COMPLICATED GEOMETRY

The distribution of the Berry curvature for the new geometry is studied in this section. The EP surface has diverse geometries when the Hamiltonian in Eq. (12) is generalized to  $f(k_x, k_y) = m - [a \cos k_x + b \cos k_y + c \cos(2k_x) + d \cos(2k_y) + s \cos k_z]$  and  $s = 2$ . On the basis of the discussion of the physical realization [127, 138], the generalized Hamiltonian could be realized by adding long-range perturbations in the  $x$  and  $y$  directions in a periodic metallic-mesh 3D photonic crystal with  $\mathcal{PT}$ -symmetric non-Hermitian elements. In Sec. VII, we discuss in detail how to realize an EP surface in the electrical circuit.

Although the geometry of the EP surface changes when the parameters  $\{m, a, b, c, d\}$  vary, the EP still maintains the following features: (i) It possesses a mirror symmetry with respect to the  $k_z = 0$  plane. (ii) The Hamiltonian still has two layers of EP surfaces, the two EP surfaces touch each other when  $\gamma = s$ , and we discuss only the lower-layer EP surface near  $k_z = 0$ . (iii) The meridional cross-sections become irregular circles rather than disks. (iv) The equatorial cross-section no longer has regular geometry, but the streamlines of the Berry curvature in the equatorial cross-section retain the feature discussed in the previous section: they are closed curves that can be depicted according to Eq. (20). To illustrate the distribution of the Berry curvature, the geometries of the EP surface under two sets of parameters are studied and the other cases share similar distributions. In the equatorial cross-section, Eq. (19) remains valid, and Figs. 5(c) and (d) depict the streamlines of the Berry curvature. The two similar equatorial cross-sections in Fig. 5(c) and (d) have five holes, and the two left or right holes are touching (separated) in (c) [(d)]. We sort the streamlines by the number and orientation of the holes they surround. Figure. 5(c) exhibits three types of streamlines surrounding one hole (the center hole, and the orientation of streamlines are anticlockwise), two holes (the two left or right holes, clockwise), and five holes (clockwise). In Fig. 5(d), in addition to the three types of streamlines, there are yet another type of streamline surrounding one hole that flows clockwise. The appearance of the new type of streamline is a consequence of the separation between the two left (or right) holes in Fig. 5(d).

In the meridional cross-section, the Berry curvature has non-zero radial and angular components and may be not perpendicular to the meridional cross-section. Berry flux is nonzero if all the arrows representing the Berry

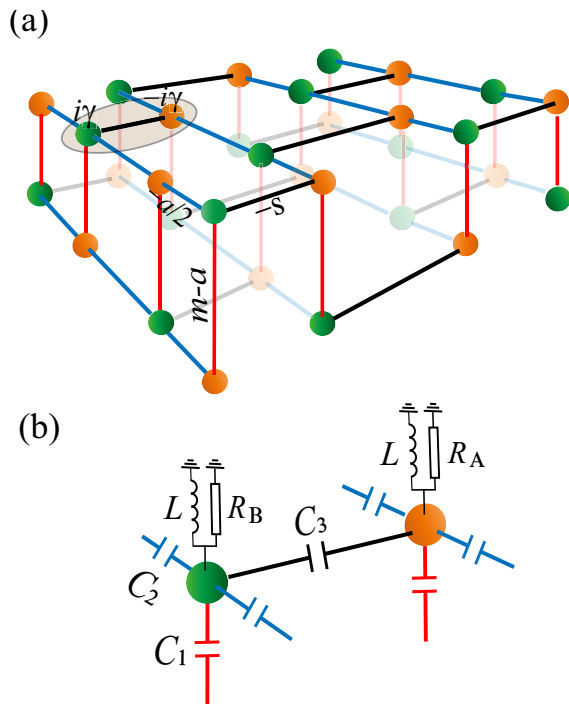


FIG. 6. (a) The schematic diagram of the tight-binding lattice in Eq. (27). The red, blue and black lines correspond to the hoppings  $m - a$ ,  $-a/2$ , and  $s$  respectively. The green and orange spheres correspond to the gain and loss. An unit cell is marked in the shadow. (b) The circuit elements of an unit cell. The red, blue and black capacitors, which are denoted with  $C_1, C_2$  and  $C_3$ , correspond to the hoppings in (a). The orange (green) node is connected to the ground by a inductance and a potentiometers  $R_A$  (negative impedance converter  $R_B$ ) which represents the gain (loss).

curvature point in the same direction in the meridional cross-section. There are specific meridional cross-sections that contain no DPs or several DPs. A natural question to ask is what the Berry curvature distribution is in these specific meridional cross-sections. A specific meridional cross-section containing no DPs is illustrated in Fig. 5(b) and the top view of this cross-section is shown in Fig. 5(d) (i.e., the yellow rectangle). In Fig. 5(f), the arrows indicate that the Berry curvature points in the positive  $x$ -direction on the left semicircle and in the negative  $x$ -direction on the right semicircle. The signs cancel out and the Berry flux vanishes. In accordance with this distribution, inside the yellow transparent rectangle in Fig. 5(d), these streamlines flow up on the right side and down on the left, and the total flux is zero. In Fig. 5(e), the non-zero winding number of the arrows indicating the Berry connection outside the EP ring is consistent with the above conclusion in Sec. IV A, which indicates that the winding number has no relation with the Berry flux.

## VII. EXPERIMENTAL SCHEME IN ELECTRICAL CIRCUIT

The EP surface can be measured using an electrical circuit which is a powerful platform for investigating topological physics [151–154]. For the sake of convenience, this section discusses the experimental scheme of EL in an electrical circuit, i.e., the intersection line of the EP surface and the  $S_V$  cross-section (see Fig. 1(b)). There are two reasons for doing this. First, the topological properties of the EL are consistent with those of the EP surface. Second, the experimental setup corresponding to the EL can be smoothly generalized to that of the EP surface due to the design flexibility of the electrical circuit.

We first show the tight-binding lattice model possessing EL. In the  $S_V$  cross-section where  $k_x = 0$ , the auxiliary field  $\mathbf{B}(\mathbf{k}) = \{B_x(\mathbf{k}), B_y(\mathbf{k})\}$  in Eq. (12) can be reduced to

$$\begin{cases} B_x = f(k_y) - s \cos k_z \\ B_y = s \sin k_z \end{cases}, \quad (25)$$

where  $f(k_y) = m - a - a \cos k_y$ , and  $s = 1$ . Substituting the Fourier transformation

$$\begin{cases} a_{k_y, k_z}^\dagger = \frac{1}{\sqrt{N}} \sum_{j,l} e^{ik_y j} e^{ik_z l} a_{j,l}^\dagger \\ b_{k_y, k_z}^\dagger = \frac{1}{\sqrt{N}} \sum_{j,l} e^{ik_y h} e^{ik_z l} b_{j,l}^\dagger \end{cases} \quad (26)$$

into the core matrix  $\sum_{k_y, k_z} \mathbf{B}(k_y, k_z) \cdot \sigma$ , we get the lattice model

$$H = \sum_{\mathbf{r}} \left( (m - a) a_{\mathbf{r}}^\dagger b_{\mathbf{r}} - \frac{a}{2} (a_{\mathbf{r}}^\dagger b_{\mathbf{r}+\hat{j}} + a_{\mathbf{r}}^\dagger b_{\mathbf{r}-\hat{j}} - sa_{\mathbf{r}}^\dagger b_{\mathbf{r}+\hat{l}}) + \text{h.c.} + i\gamma a_{\mathbf{r}}^\dagger a_{\mathbf{r}} - i\gamma b_{\mathbf{r}}^\dagger b_{\mathbf{r}} \right) \quad (27)$$

where  $\mathbf{r} = x\hat{j} + y\hat{l}$  is the position vector,  $\hat{j}, \hat{l}$  represents the unit vectors, and the system size is  $N$ . A schematic diagram of the lattice model is shown in Fig. 6(a). The hoppings  $-a/2$ ,  $m - a$  and  $-s$  are represented by the blue, red and black lines, respectively. The on-site gains and losses are shown in orange and green, respectively. We can extend this lattice system in the  $x$ -direction to obtain a model possessing an EP surface.

The lattice system can be represented by an electrical circuit with  $N$  nodes. An  $N \times N$  matrix  $J(\omega, \mathbf{r})$ , termed circuit Laplacian or admittance matrix, can be used to represent the Hamiltonian of a tight-binding model [151, 152, 155].  $J(\omega, \mathbf{r})$  describes the voltage response  $\mathbf{V}(\omega, \mathbf{r})$  to an ac input current  $\mathbf{I}(\omega, \mathbf{r})$  according to

$$\mathbf{V}(\omega, \mathbf{r}) = J(\omega, \mathbf{r})\mathbf{I}(\omega, \mathbf{r}), \quad (28)$$

where  $\omega$  is the AC driving frequency and  $r$  represents the nodes. The vector components of  $\mathbf{V}$  and  $\mathbf{I}$  correspond to the nodes or sites in the circuit. The matrix elements of  $J(\omega, \mathbf{r})$  are determined on the admittance of circuit elements between nodes or between nodes and the ground. Figure 6(b) shows a schematic diagram of the circuit elements corresponding to a unit cell. The lattice sites



are represented by circuit nodes. The variable hoppings,  $m - a$ ,  $-a/2$  and  $-s$  can be realized by tuning the capacitors  $C_1$ ,  $C_2$  and  $C_3$ , respectively. The onsite gain  $i\gamma$  or loss  $-i\gamma$  are realized using potentiometers or a negative impedance converter to ground. The admittance matrix has an alternative representation in momentum space, denoted as  $J(\omega, \mathbf{k})$ .  $J(\omega, \mathbf{k})$  can be obtained by performing  $M$  linearly independent measurements in the electrical circuit [152, 155–158], where  $M$  describes the number of inequivalent nodes in the network. Each measurement consists of a local excitation of the circuit network and a global measurement of the voltage response, from which all the components of  $J(\omega, \mathbf{k})$  can be extracted. Then EL can be obtained by diagonalizing the admittance matrix  $J(\omega, \mathbf{k})$ .

### VIII. DISCUSSION

In summary, we have investigated the distribution of Berry curvature inside the EP surface of  $\mathcal{PT}$ -symmetric 3D non-Hermitian two-band systems. The EP surface acts as the separation between the zero and non-zero Berry curvatures. Inside a torus-like EP surface, the distributions of Berry connections and curvatures in the meridional and equatorial cross-sections are discussed. In the meridional cross-section, the Berry connection serves as a planar vortex field and diverges at the DP and EP surface. The Berry curvature has only an axial component and diverges at the EP surface. In the equatorial cross-sections, the Berry curvature forms the closed curves inside the EP surface. The distributions of Berry curvature are analogous to the magnetic lines generated by the solenoid, and the EP surface can be analogous to the solenoids. On the basis of the distribution of the Berry curvature, we obtain the nonquantized Berry flux. The key to identifying the zero or non-zero Berry flux in a meridional cross-section is determining whether all the arrows indicating Berry curvatures point in the same direction. The numerical adiabatic evolution corresponds with the aforementioned analysis of the nonquantized Berry flux. We also discuss the distribution of Berry curvature in a general case in which the EP surface has more complicated geometry. In the equatorial cross-sections, the Berry curvatures retain the form of closed curves. The streamlines with arrows indicating the direction of the Berry curvature are categorized by arrow orientations and the number of the holes they surround. We discuss a scheme of realizing the EP surface in an electrical circuit. Our findings deepen understanding of EP surfaces and the topological properties of  $\mathcal{PT}$ -symmetric non-Hermitian systems.

### ACKNOWLEDGMENTS

We acknowledge the support of the National Natural Science Foundation of China (Grants No. 12374461, No.

12222504, and No. 12305018).

## APPENDIX

### A. Berry curvature in and out the nodal volume

We present detailed calculations of the component for Berry connection  $\vec{\mathcal{A}}$  and Berry curvature  $\vec{\mathcal{F}}$  according to the definitions  $\mathcal{A}_j = \text{Re}(i \langle \phi_-^L | \partial_j | \phi_-^R \rangle)$  and  $\mathcal{F}_j = \partial_l \mathcal{A}_i - \partial_i \mathcal{A}_l$ .

(1) **Outside the nodal volume** ( $\gamma^2 < B_x^2 + B_y^2$ )

**a. Berry connection.** Substitute the Eq. (4) and (5) into  $\mathcal{A}_j = \text{Re}(i \langle \phi_-^L | \partial_j | \phi_-^R \rangle)$ , which results in

$$\mathcal{A}_j = -\frac{1}{2} (\partial_j \alpha + \partial_j \beta). \quad (29)$$

Differentiate  $\tan \alpha = \gamma/\varepsilon$  where  $\varepsilon = \sqrt{B_x^2 + B_y^2 - \gamma^2}$

$$\frac{1}{\cos^2 \alpha} d\alpha = -\gamma \varepsilon^{-2} (\partial_x \varepsilon dk_x + \partial_y \varepsilon dk_y + \partial_z \varepsilon dk_z), \quad (30)$$

move  $\cos^2 \alpha$  to the right-hand side of "=" and we get

$$\partial_j \alpha = -\frac{(B_x \partial_j B_x + B_y \partial_j B_y) \gamma}{\varepsilon (B_x^2 + B_y^2)}. \quad (31)$$

A similar calculation performing for  $\tan \beta = B_y/B_x$  yields

$$\partial_j \beta = \frac{B_x \partial_j B_y - B_y \partial_j B_x}{B_x^2 + B_y^2}. \quad (32)$$

Substitute Eq. (31) and Eq. (32) into the Eq. (29), we have

$$\mathcal{A}_j = \frac{(\varepsilon B_y + \gamma B_x) \partial_j B_x + (\gamma B_y - \varepsilon B_x) \partial_j B_y}{2\varepsilon (B_x^2 + B_y^2)}. \quad (33)$$

**b. Berry curvature.** Substitute Eq. (29) into  $\mathcal{F}_j = \partial_l \mathcal{A}_i - \partial_i \mathcal{A}_l$ ,

$$\mathcal{F}_j = \frac{1}{2} [\partial_l (\partial_i \beta) - \partial_i (\partial_l \beta) + \partial_l (\partial_i \alpha) - \partial_i (\partial_l \alpha)]. \quad (34)$$

Firstly, we prove  $\partial_j (\partial_l \alpha) - \partial_l (\partial_j \alpha) = 0$ . Partial derivative of  $\partial_j \alpha$  is

$$\begin{aligned} \partial_l (\partial_j \alpha) &= \frac{\gamma (3\varepsilon^2 + \gamma^2)}{\varepsilon^3 (B_x^2 + B_y^2)^2} [B_x^2 \partial_l B_x \partial_j B_x + B_y^2 \partial_l B_y \partial_j B_y \\ &\quad + B_x B_y (\partial_l B_x \partial_j B_y + \partial_l B_y \partial_j B_x)] \\ &\quad - \frac{\gamma}{\varepsilon (B_x^2 + B_y^2)} [\partial_l B_x \partial_j B_x + B_x \partial_l (\partial_j B_x)] \\ &\quad + B_y \partial_l (\partial_j B_y) + \partial_l B_y \partial_j B_y]. \end{aligned} \quad (35)$$

$\partial_j (\partial_l \alpha)$  can be obtained by swapping  $j$  with  $l$  in Eq. (35) and  $\partial_l (\partial_j \alpha)$  has the same expression with  $\partial_j (\partial_l \alpha)$ , which means

$$\partial_l (\partial_j \alpha) - \partial_j (\partial_l \alpha) = 0. \quad (36)$$

Secondly, we prove that  $\partial_l(\partial_j\beta) - \partial_j(\partial_l\beta) = 0$ . Partial derivative of  $\partial_j\beta$  is

$$\begin{aligned} \partial_l(\partial_j\beta) &= \frac{1}{(B_x^2 + B_y^2)^2} [2B_y B_x (\partial_l B_x \partial_j B_x - \partial_l B_y \partial_j B_y) \\ &\quad + (B_y^2 - B_x^2) (\partial_l B_x \partial_j B_y + \partial_l B_y \partial_j B_x) \\ &\quad + (B_x^2 + B_y^2) (B_x \partial_l (\partial_j B_y) - B_y \partial_l (\partial_j B_x))]. \end{aligned} \quad (37)$$

$\partial_j(\partial_l\beta)$  can be obtained by swapping  $j$  with  $l$  and it is not difficult to check that  $\partial_j(\partial_l\beta) = \partial_l(\partial_j\beta)$ , which is

$$\partial_l(\partial_j\beta) - \partial_j(\partial_l\beta) = 0. \quad (38)$$

So we prove that  $\mathcal{F}_j = 0$ , i.e.  $\vec{\mathcal{F}} = \nabla \times \vec{\mathcal{A}} = 0$ .

**(2) Inside the nodal volume** ( $\gamma^2 > B_x^2 + B_y^2$ )

**a. Berry connection.** Substituting Eq. (6) and (7) into  $\mathcal{A}_j = \text{Re}(i \langle \phi^\perp | \partial_j | \phi^\perp \rangle)$ , the component of  $\vec{\mathcal{A}}$  is

$$\begin{aligned} \mathcal{A}_j &= -\text{Re} \left[ \frac{1}{\Omega} (\eta^2 \partial_j \beta + i \eta \partial_j \eta) \right] \\ &= -\frac{\eta^2}{\Omega} \partial_j \beta \\ &= \frac{(\varepsilon - \gamma) (B_x \partial_j B_y - B_y \partial_j B_x)}{2\varepsilon (B_x^2 + B_y^2)} \end{aligned} \quad (39)$$

where  $\varepsilon = \sqrt{\gamma^2 - B_x^2 - B_y^2}$ ,  $\eta = (\gamma - \varepsilon) / \sqrt{B_x^2 + B_y^2}$ , and  $\Omega = 2\eta\varepsilon / \sqrt{B_x^2 + B_y^2}$ .

**b. Berry curvature.** Differentiate  $\mathcal{A}_j$  to obtain

$$\partial_l \mathcal{A}_j = \frac{\varepsilon - \gamma}{2\varepsilon} \partial_l (\partial_j \beta) - \partial_l \left( \frac{\gamma}{2\varepsilon} \right) (\partial_j \beta). \quad (41)$$

$\partial_j \mathcal{A}_l$  can be obtained by swapping the indexes  $l \leftrightarrow j$ ,  $\partial_j \mathcal{A}_l = [\partial_j (\partial_l \beta)] (\varepsilon - \gamma) / (2\varepsilon) - \partial_j (\varepsilon^{-1}) (\gamma \partial_l \beta / 2)$ . Therefore the component of berry curvature can be calculated

$$\mathcal{F}_i = \partial_l \mathcal{A}_j - \partial_j \mathcal{A}_l = \frac{\gamma}{2\varepsilon^2} (\partial_l \varepsilon \partial_j \beta - \partial_j \varepsilon \partial_l \beta), \quad (42)$$

and Eq. (38) is used in the calculation. Then move  $\partial_j \varepsilon = -\varepsilon_k^{-1} (B_x \partial_j B_x + B_y \partial_j B_y)$  and Eq. (32) into aforementioned equation, we have

$$\partial_l \mathcal{A}_j - \partial_j \mathcal{A}_l = \frac{\gamma}{2\varepsilon^3} (\partial_l B_y \partial_j B_x - \partial_l B_x \partial_j B_y), \quad (43)$$

that is

$$\mathcal{F}_j = \partial_l \mathcal{A}_i - \partial_i \mathcal{A}_l = \frac{\gamma}{2\varepsilon^3} (\partial_l B_y \partial_i B_x - \partial_l B_x \partial_i B_y). \quad (44)$$

### B. Berry connection and curvature in the meridional cross-section

This section gives the details of calculating Eq. (14) and Eq. (16) under the constraint of condition  $0 < r < \gamma$ .

The EP surface is in the form of a torus under the condition  $m = \sqrt{(2 - \gamma) / \gamma} + 1$ ,  $a = (m - 1 +$

$\sqrt{(m - 1)^2 - \gamma^2 + 4}) / (4 - \gamma^2)$ , as presented in 1 (a). The schematic of the meridional cross-section is presented in Fig. 1 (b). The center of the circle  $\mathcal{O}(k_{y_0}, 0)$  is the DP for the Hermitian case; therefore,  $k_{y_0}$  meets the condition  $B_x(0, y_0, 0) = 0$ , which yields

$$a \cos k_{y_0} = m - a - 1, \quad (45)$$

and

$$a^2 \sin^2 k_{y_0} = (m - 1) (2a - m + 1). \quad (46)$$

Replace  $m$  and  $a$  with  $\gamma$  in Eq. (46), we have  $a \sin k_{y_0} = \pm 1$ . Here we discuss the case of  $a \sin k_{y_0} = -1$ . In polar coordinates,  $(k_y, k_z) = (k_{y_0} + r \cos \theta, r \sin \theta)$ , where  $r$  is small. Using the above parameter settings and taking the Taylor expansion, the Hamiltonian in Eq. (1) can be rewritten as

$$H = \begin{pmatrix} i\gamma & r e^{i\theta} \\ r e^{-i\theta} & -i\gamma \end{pmatrix} \quad (47)$$

and the Berry connection in Eq. (8) and Berry curvature in Eq. (9) can be reduced into

$$\begin{cases} \mathcal{A}_x = 0 \\ \mathcal{A}_y \approx \frac{\varepsilon - \gamma}{2\varepsilon r} \sin \theta \\ \mathcal{A}_z \approx -\frac{\varepsilon - \gamma}{2\varepsilon r} \cos \theta \end{cases}, \text{ and } \begin{cases} \mathcal{F}_x \approx \frac{\gamma}{2\varepsilon^3} \\ \mathcal{F}_y = \mathcal{F}_z = 0 \end{cases} \quad (48)$$

By using a coordinate transformation of

$$\begin{pmatrix} \mathcal{A}_r \\ \mathcal{A}_\theta \end{pmatrix} = S \begin{pmatrix} \mathcal{A}_y \\ \mathcal{A}_z \end{pmatrix}, \quad (49)$$

where

$$S = \begin{pmatrix} \cos \theta & \sin \theta \\ -\sin \theta & \cos \theta \end{pmatrix}, \quad (50)$$

the form for Berry connection and curvature in polar coordinates,

$$\begin{cases} \mathcal{A}_r = \mathcal{A}_x = 0 \\ \mathcal{A}_\theta = \frac{\sqrt{\gamma^2 - r^2 - \gamma}}{2\varepsilon r} \end{cases} \text{ and } \begin{cases} \mathcal{F}_r = \mathcal{F}_\theta = 0 \\ \mathcal{F}_x = \frac{\gamma}{2\varepsilon^3} \end{cases}. \quad (51)$$

can be easily obtained.

## IX. BERRY CONNECTION AND BERRY CURVATURE DEFINED UNDER THE DIRAC NORM

This section gives the expressions for the Berry connection and Berry curvature under the Dirac orthonormal basis in the broken region. As the purpose of this section is to compare the results with those obtained under the definition of biorthogonal bases sets, and the details of calculation is similar to that in Sec. VIII A, therefore only the results will be presented.

The expression for the eigenstates of the Hamiltonian in Eq. (1) is

$$|\phi_+^R\rangle = \frac{1}{\sqrt{\Lambda}} \begin{pmatrix} \eta e^{i(\frac{\pi}{2}-\beta)} \\ 1 \end{pmatrix} \quad (52)$$

corresponding to the eigenvalue  $-i\sqrt{\gamma^2 - B_x^2 - B_y^2}$ , where

$$\Lambda = \eta^2 + 1, \eta = \frac{\gamma + \sqrt{\gamma^2 - B_x^2 - B_y^2}}{\sqrt{B_x^2 + B_y^2}}. \quad (53)$$

Berry connection can be defined by

$$\vec{\mathcal{A}}_k^d = i \langle \phi_+^R | \nabla_{\vec{k}} | \phi_+^R \rangle = \mathcal{A}_{k_x}^d \mathbf{e}_x + \mathcal{A}_{k_y}^d \mathbf{e}_y + \mathcal{A}_{k_z}^d \mathbf{e}_y, \quad (54)$$

where the component reads

$$\mathcal{A}_j^d = \frac{\varepsilon + \gamma}{2\gamma(B_x^2 + B_y^2)} (B_x \partial_j B_y - B_y \partial_j B_x) \quad (55)$$

and Berry curvature can be defined by

$$\mathcal{F}_j^d = \partial_l \mathcal{A}_i^d - \partial_i \mathcal{A}_l^d = \frac{\partial_i B_y \partial_l B_x - \partial_l B_y \partial_i B_x}{2\gamma\varepsilon}. \quad (56)$$

The denominator of  $\mathcal{A}_j^d$  has one less factor of  $\varepsilon$  compared to the denominator of  $\mathcal{A}_j$  in Eq. (8), which leads a convergent  $\mathcal{A}_j^d$  at the EP surface.

- 
- [1] C. M. Bender, Making sense of non-Hermitian Hamiltonians, Rep. Prog. Phys. **70**, 947 (2007).
  - [2] N. Moiseyev, Non-Hermitian Quantum Mechanics (Cambridge University Press, Cambridge, UK, 2011).
  - [3] L. Feng, R. El-Ganainy, and L. Ge, Non-Hermitian photonics based on parity-time symmetry, Nat. Photonics **11**, 752 (2017).
  - [4] S. Longhi, Parity-time symmetry meets photonics: A new twist in non-Hermitian optics, Europhys. Lett. **120**, 64001 (2017).
  - [5] R. El-Ganainy, K. G. Makris, M. Khajavikhan, Z. H. Musslimani, S. Rotter, and D. N. Christodoulides, Non-Hermitian physics and PT symmetry, Nat. Phys. **14**, 11 (2018).
  - [6] M. A. Miri and A. Alù, Exceptional points in optics and photonics, Science **363**, eaar7709 (2019).
  - [7] S. K. Özdemir, S. Rotter, F. Nori, and L. Yang, Parity-time symmetry and exceptional points in photonics, Nat. Mater. **18**, 783 (2019).
  - [8] Y. Ashida, Z. Gong, and M. Ueda, Non-Hermitian physics, Adv. Phys. **69**, 249 (2020).
  - [9] E. J. Bergholtz, J. C. Budich, and F. K. Kunst, Exceptional topology of non-Hermitian systems, Rev. Mod. Phys. **93**, 015005 (2021).
  - [10] K. Ding, C. Fang, and G. Ma, Non-Hermitian topology and exceptional-point geometries, Nat. Rev. Phys. **4**, 745 (2022).
  - [11] P. Wang, L. Jin, G. Zhang, and Z. Song, Wave emission and absorption at spectral singularities, Phys. Rev. A **94**, 053834 (2016).
  - [12] L. Ge, Non-Hermitian lattices with a flat band and polynomial power increase, Photon. Res. **6**, A10 (2018).
  - [13] L. Jin and Z. Song, Incident direction independent wave propagation and unidirectional lasing, Phys. Rev. Lett. **121**, 073901 (2018).
  - [14] H. S. Xu and L. Jin, Pseudo-Hermiticity protects the energy-difference conservation in the scattering, Phys. Rev. Research **5**, L042005 (2023).
  - [15] L. Jin and Z. Song, Solutions of  $\mathcal{PT}$ -symmetric tight-binding chain and its equivalent Hermitian counterpart, Phys. Rev. A **80**, 052107 (2009).
  - [16] L. Jin and Z. Song, Physics counterpart of the  $\mathcal{PT}$  non-Hermitian tight-binding chain, Phys. Rev. A **81**, 032109 (2010).
  - [17] Q. Zhong, M. Khajavikhan, D. N. Christodoulides, and R. El-Ganainy, Winding around non-Hermitian singularities, Nat. Commun. **9**, 4808 (2018).
  - [18] X. L. Zhang, S. B. Wang, B. Hou, and C. T. Chan, Dynamically encircling exceptional points: in situ control of encircling loops and the role of the starting point, Phys. Rev. X **8**, 021066 (2018).
  - [19] L. Jin, Parity-time-symmetric coupled asymmetric dimers, Phys. Rev. A **97**, 012121 (2018).
  - [20] X. L. Zhang and C. T. Chan, Dynamically encircling exceptional points in a three-mode waveguide system, Commun. Phys. **2**, 63 (2019).
  - [21] S. M. Zhang, X. Z. Zhang, L. Jin, and Z. Song, High-order exceptional points in supersymmetric arrays, Phys. Rev. A **101**, 033820 (2020).
  - [22] L. Jin, H. C. Wu, B. B. Wei, and Z. Song, Hybrid exceptional point created from type-III Dirac point, Phys. Rev. B **101**, 045130 (2020).
  - [23] L. C. Xie, L. Jin, and Z. Song, Antihelical edge states in two-dimensional photonic topological metals, Sci. Bull. **68**, 255 (2023).
  - [24] H. C. Wu, H. S. Xu, L. C. Xie, and L. Jin, Edge state, band topology, and time boundary effect in the Fine-Grained categorization of Chern Insulators, Phys. Rev. Lett. **132**, 136802 (2024).
  - [25] S. Yao, F. Song, and Z. Wang, Non-Hermitian Chern bands, Phys. Rev. Lett. **121**, 136802 (2018).
  - [26] S. Yao and Z. Wang, Edge States and Topological Invariants of Non-Hermitian Systems, Phys. Rev. Lett. **121**, 086803 (2018).
  - [27] T. E. Lee, Anomalous edge state in a non-Hermitian lattice, Phys. Rev. Lett. **116**, 133903 (2016).
  - [28] L. Jin and Z. Song, Bulk-boundary correspondence in a non-Hermitian system in one dimension with chiral inversion symmetry, Phys. Rev. B **99**, 081103(R) (2019).
  - [29] S. Longhi, Non-Bloch-Band collapse and chiral zener tunneling, Phys. Rev. Lett. **124**, 066602 (2020).
  - [30] N. Okuma, K. Kawabata, K. Shiozaki, and M. Sato,

- Topological origin of non-Hermitian skin effects, *Phys. Rev. Lett.* **124** 086801 (2020).
- [31] F. Song, S. Y. Yao, and Z. Wang, Non-Hermitian skin effect and chiral damping in open quantum systems, *Phys. Rev. Lett.* **123**, 170401 (2019).
- [32] K. Zhang, Z. Yang, and C. Fang, Universal non-Hermitian skin effect in two and higher dimensions, *Nat. Commun.* **13**, 2496 (2022).
- [33] Q. Liang, D. Xie, Z. Dong, H. Li, H. Li, B. Gadway, W. Yi, and B. Yan, Dynamic signatures of non-Hermitian skin effect and topology in ultracold Atoms, *Phys. Rev. Lett.* **129**, 070401 (2022).
- [34] L. L. Wan and X. Y. Lü, Quantum-Squeezing-Induced Point-Gap topology and skin effect, *Phys. Rev. Lett.* **130**, 203605 (2023).
- [35] K. Cao, Q. Du, and S. P. Kou, Many-body non-Hermitian skin effect at finite temperatures, *Phys. Rev. B* **108**, 165420 (2023).
- [36] L. Xiao, T. Deng, K. Wang, Z. Wang, W. Yi, and P. Xue, Observation of non-Bloch parity-time symmetry and exceptional points, *Phys. Rev. Lett.* **126**, 230402 (2021).
- [37] Z. Yang, K. Zhang, C. Fang, and J. Hu, Non-Hermitian bulk-boundary correspondence and auxiliary generalized Brillouin zone theory, *Phys. Rev. Lett.* **125**, 226402 (2020).
- [38] H. C. Wu, L. Jin, and Z. Song, Inversion symmetric non-Hermitian Chern insulator, *Phys. Rev. B* **100**, 155117 (2019).
- [39] F. Song, S. Y. Yao, and Z. Wang, Non-Hermitian topological invariants in real space, *Phys. Rev. Lett.* **123**, 246801 (2019).
- [40] Dan S. Borgnia, A. J. Kruchkov, and R. J. Slager, Non-Hermitian boundary modes and topology, *Phys. Rev. Lett.* **124**, 056802 (2020).
- [41] K. Zhang, Z. Yang, and C. Fang, Correspondence between winding numbers and skin modes in non-Hermitian systems, *Phys. Rev. Lett.* **125**, 126402 (2020).
- [42] Y. Yi and Z. Yang, Non-Hermitian skin modes induced by on-site dissipations and chiral tunneling effect, *Phys. Rev. Lett.* **125**, 186802 (2020).
- [43] Z. Gong, Y. Ashida, K. Kawabata, K. Takasan, S. Higashikawa, and M. Ueda, Topological Phases of Non-Hermitian Systems, *Phys. Rev. X* **8**, 031079 (2018).
- [44] H. Shen, B. Zhen, and L. Fu, Topological band theory for non-Hermitian Hamiltonians, *Phys. Rev. Lett.* **120**, 146402 (2018).
- [45] Y. Xu, S. T. Wang, and L. M. Duan, Weyl exceptional rings in a three-dimensional dissipative cold atomic gas, *Phys. Rev. Lett.* **118**, 045701 (2017).
- [46] D. Leykam, K. Y. Bliokh, C. L. Huang, Y. D. Chong, and F. Nori, Edge Modes, degeneracies, and topological numbers in non-Hermitian systems, *Phys. Rev. Lett.* **118**, 040401 (2017).
- [47] K. Yokomizo and S. Murakami, Non-Bloch band theory of non-Hermitian systems, *Phys. Rev. Lett.* **123**, 066404 (2019).
- [48] Z. Y. Ge, Y. R. Zhang, T. Liu, S. W. Li, H. Fan, and F. Nori, Topological band theory for non-Hermitian systems from the Dirac equation, *Phys. Rev. B* **100**, 054105 (2019).
- [49] K. L. Zhang, H. C. Wu, L. Jin, and Z. Song, Topological phase transition independent of system non-Hermiticity, *Phys. Rev. B* **100**, 045141 (2019).
- [50] Y. Ke, J. Huang, W. Liu, Y. Kivshar, and C. Lee, Topological inverse band theory in waveguide quantum Electrodynamics, *Phys. Rev. Lett.* **131**, 103604 (2023).
- [51] L. H. Li, C. H. Lee, and J. B. Gong, Geometric characterization of non-Hermitian topological systems through the singularity ring in pseudospin vector space, *Phys. Rev. B* **100**, 075403 (2019).
- [52] X. M. Yang, P. Wang, L. Jin, and Z. Song, Visualizing topology of real-energy gapless phase arising from exceptional point, *J. Phys. Commun.* **4**, 095005 (2020).
- [53] H. C. Wu, X. M. Yang, L. Jin, and Z. Song, Untying links through anti-parity-time-symmetric coupling, *Phys. Rev. B* **102**, 161101(R) (2020).
- [54] K. Y. Bliokh, D. Leykam, M. Lein, and F. Nori, Topological non-Hermitian origin of surface Maxwell waves, *Nat. Commun.* **10**, 580 (2019).
- [55] Z. Xu, R. Zhang, S. Chen, L. Fu, and Y. Zhang, Fate of zero modes in a finite Su-Schrieffer-Heeger model with PT symmetry, *Phys. Rev. A* **101**, 013635 (2020).
- [56] W. J. Xi, Z. H. Zhang, Z. C. Gu, and W. Q. Chen, Classification of topological phases in one dimensional interacting non-Hermitian systems and emergent unitarity, *Sci. Bull.* **66**, 1731 (2021).
- [57] C. C. Wojcik, X. Q. Sun, T. Bzdusek, and S. H. Fan, Topological classification of non-Hermitian Hamiltonians, *Phys. Rev. B* **101**, 205417 (2020).
- [58] F. Yang, Z. Wei, X. Tong, K. Cao, and S. P. Kou, Symmetry classes of dissipative topological insulators with edge dark states, *Phys. Rev. B* **107**, 165139 (2023).
- [59] H. Zhou and J. Y. Lee, Periodic table for topological bands with non-Hermitian symmetries, *Phys. Rev. B* **99**, 235112 (2019).
- [60] K. Kawabata, K. Shiozaki, M. Ueda, and M. Sato, Symmetry and topology in non-Hermitian physics, *Phys. Rev. X* **9**, 041015 (2019).
- [61] K. Kawabata, T. Bessho, and M. Sato, Classification of exceptional points and non-Hermitian topological semimetals, *Phys. Rev. Lett.* **123**, 066405 (2019).
- [62] K. Kawabata, S. Higashikawa, Z. P. Gong, Y. Ashida, and M. Ueda, Topological unification of time-reversal and particle-hole symmetries in non-Hermitian physics, *Nat. Commun.* **10**, 297 (2019).
- [63] T. Yoshida, I. Danshita, R. Peters, and Norio Kawakami, Reduction of topological Z classification in Cold-Atom systems, *Phys. Rev. Lett.* **121**, 025301 (2018).
- [64] C. H. Lee, L. Li, R. Thomale, and J. Gong, Unraveling non-Hermitian pumping: emergent spectral singularities and anomalous responses, *Phys. Rev. B* **102**, 085151 (2020).
- [65] H. Park, S. Wong, A. Bouhon, R. J. Slager, and S. S. Oh, Topological phase transitions of non-Abelian charged nodal lines in spring-mass systems, *Phys. Rev. B* **105**, 214108 (2022).
- [66] J. P. Hou, Y. J. Wu, and C. W. Zhang, Two-dimensional non-Hermitian topological phases induced by asymmetric hopping in a one-dimensional superlattice, *Phys. Rev. A* **103**, 033305 (2021).
- [67] J. P. Hou, Y. J. Wu, and C. W. Zhang, Non-Hermitian topological phase transitions for quantum spin Hall insulators, *Phys. Rev. B* **103**, 205110 (2021).
- [68] S. Longhi, Topological phase transition in non-Hermitian quasicrystals, *Phys. Rev. Lett.* **122**, 237601 (2019).



- [69] Z. Lei, Y. Deng, C. Lee, Symmetry-Protected topological phase for Spin-Tensor-Momentum-Coupled Ultracold atoms, *Phys. Rev. A* **102**, 013301 (2020).
- [70] D. Leykam, S. Flach, and Y. D. Chong, Flat bands in lattices with non-Hermitian coupling, *Phys. Rev. B* **96**, 064305 (2017).
- [71] Y. Liu and S. Chen, Diagnosis of bulk phase diagram of non-reciprocal topological lattices by impurity modes, *Phys. Rev. B* **102**, 075404 (2020).
- [72] C. Qin, B. Wang, Z. J. Wong, S. Longhi, and P. Lu, Discrete diffraction and Bloch oscillations in non-Hermitian frequency lattices induced by complex photonic gauge fields, *Phys. Rev. B* **101**, 064303 (2020).
- [73] L. C. Xie, H. C. Wu, X. Z. Zhang, L. Jin, and Z. Song, Two-dimensional anisotropic non-Hermitian Lieb lattice, *Phys. Rev. B* **104**, 125406 (2021).
- [74] X. Tong, G. Xianlong, and S. P. Kou, Adiabatic-impulse approximation in the non-Hermitian Landau-Zener model, *Phys. Rev. B* **107**, 104306 (2023).
- [75] D. W. Zhang, Y. L. Chen, G. Q. Zhang, L. J. Lang, Z. Li, and S. L. Zhu, Skin superfluid, topological Mott insulators, and asymmetric dynamics in interacting non-Hermitian Aubry-Andre-Harper models, *Phys. Rev. B* **101**, 235150 (2020).
- [76] Q. B. Zeng, Y. B. Yang, and Y. Xu, Topological phases in non-Hermitian Aubry-André-Harper models, *Phys. Rev. B* **101**, 020201(R) (2020).
- [77] L. Jin, P. Wang, and Z. Song, Su-Schrieffer-Heeger chain with one pair of  $\mathcal{PT}$ -symmetric defects, *Sci. Rep.* **7**, 5903 (2017).
- [78] L. Jin, Topological phases and edge states in a non-Hermitian trimerized optical lattice, *Phys. Rev. A* **96**, 032103 (2017).
- [79] Z. Oztas and N. Candemir, Su-Schrieffer-Heeger model with imaginary gauge field, *Phys. Lett. A* **383**, 1821 (2019).
- [80] C. Yuce and H. Ramezani, Topological states in a non-Hermitian two-dimensional Su-Schrieffer-Heeger model, *Phys. Rev. A* **100**, 032102 (2019).
- [81] H. Jiang, R. Lu, and S. Chen, Topological invariants, zero mode edge states and nite size effect for a generalized non-reciprocal Su-Schrieffer-Heeger model, *Eur. Phys. J. B* **93**, 125 (2020).
- [82] H. C. Wu, L. Jin, and Z. Song, Topology of an anti-parity-time symmetric non-Hermitian Su-Schrieffer-Heeger model, *Phys. Rev. B* **103**, 235110 (2021).
- [83] D. W. Zhang, L. Z. Tang, L. J. Lang, H. Yan, and S. L. Zhu, Non-Hermitian topological anderson insulators, *Sci. China Phys. Mech. Astron.* **63**, 267062 (2020).
- [84] S. Longhi, Metal-insulator phase transition in a non-Hermitian Aubry-André-Harper model, *Phys. Rev. B* **100**, 125157 (2019).
- [85] C. Yuce and H. Ramezani, Robust exceptional points in disordered systems, *Europhys. Lett.* **126**, 17002 (2019).
- [86] X. W. Luo and C. Zhang, Photonic topological insulators induced by non-Hermitian disorders in a coupled-cavity array, *Appl. Phys. Lett.* **123**, 081111 (2023).
- [87] Z. Q. Zhang, H. Liu, H. Liu, H. Jiang, and X. C. Xie, Bulk-boundary correspondence in disordered non-Hermitian systems, *Sci. Bull.* **68**, 157 (2023).
- [88] M. S. Rudner and L. S. Levitov, Topological Transition in a Non-Hermitian Quantum Walk, *Phys. Rev. Lett.* **102**, 065703 (2009).
- [89] L. Zhou and J. Gong, Non-Hermitian Floquet topological phases with arbitrarily many real-quasienergy edge states, *Phys. Rev. B* **98**, 205417 (2018).
- [90] R. de J. León-Montiel, Mario A. Quiroz-Juárez, J. L. Domínguez-Juárez, R. Quintero-Torres, J. L. Aragón, A. K. Harter, and Y. N. Joglekar, Observation of slowly decaying eigenmodes without exceptional points in Floquet dissipative synthetic circuits, *Commun. Phys.* **1**, 88 (2018).
- [91] S. Longhi, Non-Bloch  $\mathcal{PT}$ -symmetry breaking in non-Hermitian photonic quantum walks, *Opt. Lett.* **44**, 5804 (2019).
- [92] B. Wang, T. Chen, and X. D. Zhang, Topological photonics: Observation of novel robust edge states in dissipative non-Hermitian quantum walks, *Laser Photonics Rev.* **14**, 202070041 (2020).
- [93] S. Panahiyan and S. Fritzsche, Controllable simulation of topological phases and edge states with quantum walk, *Phys. Lett. A* **384**, 126828 (2020).
- [94] L. W. Zhou, Dynamical characterization of non-Hermitian Floquet topological phases in one dimension, *Phys. Rev. B* **100**, 184314 (2019).
- [95] L. W. Zhou, Non-Hermitian Floquet topological superconductors with multiple Majorana edge modes, *Phys. Rev. B* **101**, 014306 (2020).
- [96] B. Zhu, H. H. Zhong, J. Jia, F. Q. Ye, and L. B. Fu, Floquet control of global  $\mathcal{PT}$  symmetry in 2D arrays of quadrimer waveguides, *Phys. Rev. A* **102**, 053510 (2020).
- [97] X. Z. Zhang and J. B. Gong, Non-Hermitian Floquet topological phases: Exceptional points, coalescent edge modes, and the skin effect, *Phys. Rev. B* **101**, 045415 (2020).
- [98] C. Liu, H. Hu, and S. Chen, Symmetry and topological classification of Floquet non-Hermitian systems, *Phys. Rev. B* **105**, 214305 (2022).
- [99] C. H. Lee and R. Thomale, Anatomy of skin modes and topology in non-Hermitian systems, *Phys. Rev. B* **99**, 201103 (2019).
- [100] X. W. Luo and C. W. Zhang, Higher-Order topological corner states induced by gain and loss, *Phys. Rev. Lett.* **123**, 073601 (2019).
- [101] M. Ezawa, Non-Hermitian higher-order topological states in nonreciprocal and reciprocal systems with their electric-circuit realization, *Phys. Rev. B* **99**, 201411(R) (2019).
- [102] T. Liu, Y. R. Zhang, Q. Ai, Z. P. Gong, K. Kawabata, M. Ueda, and F. Nori, Second-Order topological phases in non-Hermitian systems, *Phys. Rev. Lett.* **122**, 076801 (2019).
- [103] Y. J. Wu, C. C. Liu, and J. Hou, Wannier-type photonic higher-order topological corner states induced solely by gain and loss, *Phys. Rev. A* **101**, 043833 (2020).
- [104] K. Kudo, T. Yoshida, and Y. Hatsugai, Higher-order topological Mott insulators, *Phys. Rev. Lett.* **123**, 196402 (2019).
- [105] X. Zhang and M. Franz, Non-Hermitian exceptional Landau quantization in electric circuits, *Phys. Rev. Lett.* **124**, 046401 (2020).
- [106] R. Chen, C. Z. Chen, B. Zhou, and D. H. Xu, Finite-size effects in non-Hermitian topological systems, *Phys. Rev. B* **99**, 155431 (2019).
- [107] P. Y. Chang, J. S. You, X. D. Wen, and S. Ryu, Entanglement spectrum and entropy in topological non-Hermitian systems and non-unitary conformal field the-

- ories, Phys. Rev. Research **2**, 033069 (2020).
- [108] E. Lee, H. Lee, and B. J. Yang, Many-body approach to non-Hermitian physics in fermionic systems, Phys. Rev. B **101**, 121109(R) (2020).
- [109] Q. B. Zeng, Y. B. Yang, and R. Lü, Topological phases in one-dimensional nonreciprocal superlattices, Phys. Rev. B **101**, 125418 (2020).
- [110] Z. Xu and S. Chen, Topological Bose-Mott insulators in one-dimensional non-Hermitian superlattices, Phys. Rev. B **102**, 035153 (2020).
- [111] L. Herviou, N. Regnault, J. H. Bardarson, Entanglement spectrum and symmetries in non-Hermitian fermionic non-interacting models, SciPost Phys. **7**, 069 (2019).
- [112] L. Du, J. H. Wu, M. Artoni, and G. C. La Rocca, Fractional quantum transport and staggered topological transition in a lossy trimerized lattice, Phys. Rev. A **100**, 052102 (2019).
- [113] C. Yuce, Spontaneous topological pumping in non-Hermitian systems, Phys. Rev. A **99**, 032109 (2019).
- [114] Z. O. Turker and C. Yuce, Open and closed boundaries in non-Hermitian topological systems, Phys. Rev. A **99**, 022127 (2019).
- [115] X. Yang, Y. Cao, and Y. Zhai, Non-Hermitian Weyl semimetals: non-Hermitian skin effect and non-Bloch Bulk-Boundary correspondence, Chin. Phys. B, **31**, 010308 (2022).
- [116] L. Xiao, K. Wang, X. Zhan, Z. Bian, K. Kawabata, M. Ueda, W. Yi, and P. Xue, Observation of critical phenomena in Parity-Time-Symmetric quantum dynamics, Phys. Rev. Lett. **123**, 230401 (2019).
- [117] K. Wang, X. Qiu, L. Xiao, X. Zhan, Z. Bian, B. C. Sanders, W. Yi, and P. Xue, Observation of emergent momentum-time skyrmions in parity-time-symmetric non-unitary quench dynamics, Nat. Commun. **10**, 2293 (2019).
- [118] K. Cao and S. P. Kou, Statistical mechanics for non-Hermitian quantum systems, Phys. Rev. Research **5**, 033196 (2023).
- [119] Z. Wang, X. T. Zeng, Y. Biao, Z. Yan, and R. Yu, Realization of a Hopf insulator in circuit systems, Phys. Rev. Lett. **130**, 057201 (2023).
- [120] B. Zhen, C. W. Hsu, Y. Igarashi, L. Lu, I. Kaminer, A. Pick, S. L. Chua, J. D. Joannopoulos, and M. Soljačić, Spawning rings of exceptional points out of Dirac cones, Nature **525**, 354 (2015).
- [121] A. Cerjan, M. Xiao, L. Q. Yuan, and S. H. Fan, Effects of non-Hermitian perturbations on Weyl Hamiltonians with arbitrary topological charges, Phys. Rev. B **97**, 075128 (2018).
- [122] X. Z. Zhang, G. Zhang, and Z. Song, Classical correspondence of the exceptional points in the finite non-Hermitian system, J. Phys. A: Math. Theor. **52**, 165302 (2018).
- [123] A. Cerjan, S. Huang, K. P. Chen, Y. Chong, and M. C. Rechtsman, Experimental realization of a Weyl exceptional ring, Nat. Photon. **13**, 623 (2019).
- [124] T. Yoshida, R. Peters, N. Kawakami, and Y. Hatsugai, Symmetry-protected exceptional rings in two-dimensional correlated systems with chiral symmetry, Phys. Rev. B **99**, 121101(R) (2019).
- [125] K. Wang, L. Xiao, J. C. Budich, W. Yi, and P. Xue, Simulating exceptional non-Hermitian metals with single-photon interferometry, Phys. Rev. Lett. **127**, 026404 (2021).
- [126] R. Okugawa and T. Yokoyama, Topological exceptional surfaces in non-Hermitian systems with parity-time and parity-particle-hole symmetries, Phys. Rev. B **99**, 041202(R) (2019).
- [127] H. Y. Zhou, J. Y. Lee, S. Liu, and B. Zhen, Exceptional surfaces in  $\mathcal{PT}$ -symmetric non-Hermitian photonic systems, Optica **6**, 190 (2019).
- [128] J. C. Budich, J. Carlstrom, F. K. Kunst, and E. J. Bergholtz, Symmetry-protected nodal phases in non-Hermitian systems, Phys. Rev. B **99**, 041406(R) (2019).
- [129] Q. Zhong, J. Ren, M. Khajavikhan, D. N. Christodoulides, S. K. Ozdemir, and R. El-Ganainy, Sensing with exceptional surfaces in order to combine sensitivity with robustness, Phys. Rev. Lett. **122**, 153902 (2019).
- [130] K. Yamamoto, M. Nakagawa, K. Adachi, K. Takasan, M. Ueda, and N. Kawakami, Theory of non-Hermitian fermionic superfluidity with a complex-valued interaction, Phys. Rev. Lett. **123**, 123601 (2019).
- [131] K. Kimura, T. Yoshida, and N. Kawakami, Chiral-symmetry protected exceptional torus in correlated nodal-line semimetals, Phys. Rev. B **100**, 115124 (2019).
- [132] X. Zhang, K. Ding, X. Zhou, J. Xu, and D. Jin, Experimental observation of an exceptional surface in synthetic dimensions with Magnon polaritons, Phys. Rev. Lett. **123**, 237202 (2019).
- [133] H. S. Xu and L. Jin, Coherent resonant transmission, Phys. Rev. Research **4**, L032015 (2022).
- [134] L. Jin and Z. Song, Symmetry-Protected scattering in non-Hermitian linear systems, Chin. Phys. Lett. **38**, 024202 (2021).
- [135] C. Fang, H. M. Weng, X. Dai, and Z. Fang, Topological nodal line semimetals, Chin. Phys. B **25**, 117106 (2016).
- [136] C. K. Chiu, J. C. Y. Teo, A. P. Schnyder, S. Ryu, Classification of topological quantum matter with symmetries, Rev. Mod. Phys. **88**, 035005 (2016).
- [137] X. Z. Zhang and Z. Song, Partial topological Zak phase and dynamical confinement in a non-Hermitian bipartite system, Phys. Rev. A **99**, 012113 (2019).
- [138] Q. H. Yan, R. J. Liu, Z. B. Yan, B. Y. Liu, H. S. Chen, Z. Wang, and L. Lu, Experimental discovery of nodal chains, Nat. Phys. **14**, 461 (2018).
- [139] R. Su, E. Estrecho, D. Biegańska, Y. Huang, M. Wurdack, M. Pieczarka, A. G. Truscott, T. C. H. Liew, E. A. Ostrovskaya, Q. Xiong, Direct measurement of a non-Hermitian topological invariant in a hybrid light-matter system, Sci. Adv. **7**, eabj8905 (2021).
- [140] G. P. Alexander, B. G. Chen, E. A. Matsumoto, and R. D. Kamien, Disclination loops, point defects, and all that in nematic liquid crystals, Rev. Mod. Phys. **84**, 497 (2012).
- [141] A. Bouhon, Q. Wu, R. J. Slager, H. Weng, O. V. Yazyev, and T. T. Bzdusek, Non-Abelian reciprocal braiding of Weyl nodes and its manifestation in ZrTe, Nat. Phys. **16**, 1137 (2020).
- [142] A. J. Beekman, J. Nissinen, K. Wu, K. Liu, R. J. Slager, Z. Nussinov, V. Cvetkovic, J. Zaanen, Dual gauge field theory of quantum liquid crystals in two dimensions, Phys. Rep. **683**, 1 (2017).
- [143] K. Liu, J. Nissinen, J. de Boer, R. J. Slager, and J. Zaanen, Hierarchy of orientational phases and axial anisotropies in the gauge theoretical description of

- generalized nematic liquid crystals, *Phys. Rev. E* **95**, 022704 (2017).
- [144] K. Liu, J. Nissinen, R. J. Slager, K. Wu, and J. Zaanen, Generalized liquid crystals: Giant fluctuations and the vestigial chiral order of  $I$ ,  $O$ , and  $T$  Matter, *Phys. Rev. X* **6**, 041025 (2016).
- [145] X. L. Qi, and S. C. Zhang, Spin-charge separation in the quantum spin Hall state, *Phys. Rev. Lett.* **101**, 086802 (2008).
- [146] V. Juričić, A. Mesaros, R. J. Slager, and J. Zaanen, Universal probes of two-dimensional topological insulators: dislocation and  $\pi$  flux, *Phys. Rev. Lett.* **108**, 106403 (2012).
- [147] B. Roy, R. J. Slager, and V. Juričić, Global Phase diagram of a dirty Weyl liquid and emergent superuniversality, *Phys. Rev. X* **8** 031076 (2018).
- [148] S. Chen, A. Bouhon, R. J. Slager, and B. Monserrat, Non-Abelian braiding of Weyl nodes via symmetry-constrained phase transitions, *Phys. Rev. B* **105**, L081117 (2022).
- [149] G. F. Lange, A. Bouhon, B. Monserrat, and R. J. Slager, Topological continuum charges of acoustic phonons in two dimensions and the Nambu-Goldstone theorem, *Phys. Rev. B* **105**, 064301 (2022).
- [150] S. Lin, L. Jin, and Z. Song, Symmetry protected topological phases characterized by isolated exceptional points, *Phys. Rev. B* **99**, 165148 (2019).
- [151] C. H. Lee, S. Imhof, C. Berger, F. Bayer, J. Brehm, L. W. Molenkamp, T. Kiessling, and R. Thomale, Topolectrical circuits, *Commun. Phys.* **1**, 39 (2018).
- [152] T. Helbig, T. Hofmann, S. Imhof, M. Abdelghany, T. Kiessling, L. W. Molenkamp, C. H. Lee, A. Szameit, M. Greiter and R. Thomale, Generalized bulk-boundary correspondence in non-Hermitian topolectrical circuits, *Nat. Phys.* **16**, 747 (2020).
- [153] X. Zhang, B. Zhang, H. Sahin, Z. B. Siu, S. M. Rafi-Ul-Islam, J. F. Kong, B. Shen, M. B. A. Jalil, R. Thomale, and C. H. Lee, Anomalous fractal scaling in two-dimensional electric networks, *Commun. Phys.* **6**, 151 (2023).
- [154] H. Zhang, T. Chen, L. Li, C. H. Lee, and X. Zhang, Electrical circuit realization of topological switching for the non-Hermitian skin effect, *Phys. Rev. B* **107**, 085426 (2023).
- [155] A. Stegmaier, S. Imhof, T. Helbig, T. Hofmann, C. H. Lee, M. Kremer, A. Fritzsche, T. Feichtner, S. Klemmt, S. Höfling, I. Boettcher, I. C. Fulga, L. Ma, O. G. Schmidt, M. Greiter, T. Kiessling, A. Szameit, and R. Thomale, Topological defect engineering and  $\mathcal{PT}$  symmetry in non-Hermitian electrical circuits, *Phys. Rev. Lett.* **126**, 215302 (2021).
- [156] T. Helbig, T. Hofmann, C. H. Lee, R. Thomale, S. Imhof, L. W. Molenkamp, and T. Kiessling, Band structure engineering and reconstruction in electric circuit networks, *Phys. Rev. B* **99**, 161114 (2019).
- [157] C. H. Lee, A. Sutrisno, T. Hofmann, T. Helbig, Y. Liu, Y. S. Ang, L. K. Ang, X. Zhang, M. Greiter, and R. Thomale, Imaging nodal knots in momentum space through topolectrical circuits, *Nat. Commun.* **11**, 4385 (2020).
- [158] H. Park, W. Gao, X. Zhang, and S. S. Oh, Nodal lines in momentum space: topological invariants and recent realizations in photonic and other systems, *Nanophotonics* **11**, 2779 (2022).